Wafer-scale single-crystalline graphene transferred from SiC exhibiting Landau quantization

Carbon 260 (2026) 121963

Contents lists available at ScienceDirect

Carbon

journal homepage: www.elsevier.com/locate/carbon

Research paper

Wafer-scale single-crystalline graphene transferred from SiC exhibiting Landau quantization

Johanna Udén [a], Joyal Jain Palakulam [a], Awse Salha [a], Per Hyldgaard [a], Elsebeth Schröder [a], Magnus Hårdensson Berntsen [b], Maciej Dendzik [b], Wanyu Chen [b], Oscar Tjernberg [b], Manasi Shah [c], Rodrigo Martinez-Duarte [c], Hans He [d], Johannes Hofmann [e,f], Thilo Bauch [a], Naveen Shetty [a], Samuel Lara-Avila [a,*]

[a] Department of Microtechnology and Nanoscience, Chalmers University of Technology, Gothenburg, SE-412 96, Sweden
[b] Department of Applied Physics, KTH Royal Institute of Technology, Stockholm, SE-114 19, Sweden
[c] Department of Mechanical Engineering, Clemson University, Clemson, SC, 29634-0921, USA
[d] RISE – Research Institutes of Sweden, Borås, SE-501 15, Sweden
[e] Department of Physics, University of Gothenburg, Gothenburg, SE-412 96, Sweden
[f] Nordita, Stockholm University and KTH Royal Institute of Technology, Stockholm, SE-106 91, Sweden

ARTICLE INFO

Keywords:
Graphene
Epitaxial graphene
Wafer-scale
Single crystal
Delamination
Quantum Hall effect

ABSTRACT

Producing large-area single-crystalline graphene is key to realizing its full potential in advanced applications, including twistronics. Yet, controlling graphene growth kinetics to avoid grain boundaries or multilayer growth remains challenging. Here, we demonstrate the possibility to obtain single-crystalline graphene free of multilayer domains via a facile one-step delamination of epitaxial graphene from silicon carbide (SiC). We find that this is enabled by a specific surface reconstruction of 4H-SiC(0001) that we achieve under our growth conditions. The high crystalline quality of graphene after delamination and transfer from the SiC substrate is confirmed by the observation of key fingerprints of Dirac fermions in quantum transport: ambipolar charge transport, Shubnikov–de Haas oscillations up to filling factor $\nu = 4N + 2 = 74$, with N the Landau index, Berry phase of π, and half-integer quantum Hall effect in cm-sized crystals. The scalability of our process, explored with recycled 4"-SiC wafers, represents an advance toward large-scale integration of high-performance graphene applications.

1. Introduction

Realizing scalable applications of two-dimensional (2D) materials in electronics, photonics, and quantum technologies requires large-area single-crystalline films [1]. In the atomically thin limit, grain boundaries strongly affect 2D material properties: they lower carrier mobility (detrimental for high-performance electronics) [2] and mechanical strength [3], increase chemical reactivity (compromising robustness to harsh processing conditions) [4], and introduce material property variability that complicates reproducible device manufacturing [5]. Significant progress in synthesizing large-area single crystals, particularly graphene, has been achieved using chemical vapor deposition (CVD) [6,7]. A driving force behind this progress is the versatility of the grown material in being transferable to virtually any substrate. Yet, key challenges in scalable CVD growth of single-crystalline graphene include an extensive parameter space for growth optimization (e.g., controlling nucleation of carbon atoms and domain growth), and the requirement to develop and use expensive single-crystalline metal catalysts to template the assembly of carbon atoms [6,7]. In contrast, epitaxial graphene (epigraphene) growth on silicon carbide (SiC) capitalizes on the commercial availability of single-crystalline SiC substrates, resulting in large-area single-crystalline graphene layers [8–10]. However, the delamination and transfer of graphene from SiC remains less explored. So far, successful attempts have not revealed the Dirac nature of the transferred material [10–13], and have faced two grand challenges: (i) material degradation due to the harsh delamination and transfer process results in defected graphene with low carrier mobilities [11,12], and (ii) multilayer graphene domains (i.e., graphene patches) – a ubiquitous defect in epigraphene – co-transfer with the top graphene layer [10,13]. The presence of excess graphene layers, cumbersome to control also in CVD growth, causes electronic inhomogeneity that limits

* Corresponding author.
E-mail address: samuel.lara@chalmers.se (S. Lara-Avila).

https://doi.org/10.1016/j.carbon.2026.121963
Received 30 June 2026; Received in revised form 5 August 2026; Accepted 6 August 2026
Available online 12 August 2026

high-performance applications [14]. Furthermore, for future twisted-layer devices, avoiding grain boundaries and multilayer patches is essential [15].

Here, we demonstrate the possibility to produce multilayer patch-free large-area graphene single-crystals by selectively delaminating the topmost graphene layer grown on SiC, while preserving its high electronic quality. Importantly, this relaxes the need for complex graphene growth optimization – via epitaxial or CVD methods – aiming to suppress multilayer growth and grain boundaries. We verify the quality of the transferred monolayer using a wide array of techniques, including electrical transport measurements. Remarkably, we observe the half-integer quantum Hall effect in centimeter-scale samples. This confirms that the high electronic quality and single-crystallinity of the transferred graphene is preserved, because the presence of grain boundaries or excessive disorder would prevent exact Hall quantization [16,17].

2. Methods

Growth of graphene

Epitaxial graphene on silicon carbide (epigraphene) was grown in tight-confinement conditions by thermal decomposition of the silicon-terminated face (0001) of single-crystalline 4H-SiC. The samples were grown in an atmosphere of argon at 800 mbar, in the range of 1750 °C–1950 °C, for 5 min [18]. The monolayer coverage of the graphene samples was determined from transmission mode micrographs with gamma correction [14]. Graphene was grown on 7 mm × 7 mm-chips or 4''-sized wafers, 4'' being the largest size possible to fit inside our growth reactor. Graphene was grown three times on the same wafers by removing graphene with oxygen plasma after each growth; the best result is obtained by re-polishing wafers.

Transfer of graphene

Metal films (gold, silver or nickel) were deposited on the surface of as-grown epigraphene using an electron beam evaporator (Lesker PVD 225) at a base pressure of 5×10^{-7} Torr, with deposition rate $R = 1$ Å s^{-1}. Metal thicknesses used for the experiments include 20, 50, 100 and 200 nm. Graphene delamination occurs in all cases, but thicker films provide better mechanical stability for successful transfer. After metal deposition, the samples were spin-coated with PMMA (polymethylmethacrylate) resist (350 nm), and post-baked at $T = 170$ °C for $t = 5$ minutes. The polymer/metal/graphene layer was peeled off from the SiC substrate by hand using thermal release tape (Nitto Denko Corp.) with release temperature $T_{release} = 120$ °C or 170 °C, and deposited on the target substrate upon heating to $T > T_{release}$. PMMA was removed using oxygen plasma or heated acetone, after which the metal layer on top of the transferred graphene was removed using liquid metal etching.

Device fabrication

Electrical devices were fabricated on graphene transferred onto SiO_2/Si (285 nm oxide thickness) using standard electron beam lithography, where electrical contacts were fabricated using physical vapor deposition of 5 nm Ti followed by 95 nm Au. For chip-sized devices, contacts were evaporated through a shadow mask. After fabrication of the devices, they were spin-coated with a layer of at least 100 nm PMMA as encapsulating layer before measurements.

Atomic force microscopy of graphene

Atomic force microscopy was performed in standard tapping mode or Peak Force tapping mode using a Bruker Dimension Icon AFM. The tip RTESP-300 was used (n-doped silicon) with resonance frequency $f_0 = 300$ Hz and spring constant $k = 40$ N/m.

Optical mapping of graphene wafer

A wafer of graphene on SiO_2/Si (Fig. 4c) was optically mapped using a Nikon L200ND automatic microscope with a 50X objective, and the bilayer content on the graphene was determined using image post-processing (thresholding using e.g., the software ImageJ).

Electrical measurements

Electrical measurements were carried out using a Physical Property Measurement System (PPMS) from Quantum Design, at temperatures from $T = 300$ K to 2 K, and magnetic fields up to $B = 14$ T. Samples were biased with a DC current of 10 nA or 100 nA for small Hall bars, and 100 nA–30 μA for large (5 mm × 5 mm) graphene devices using a Keithley 6211 current source, and sample voltages were measured using an Agilent 34420 A nanovolt meter. The electrostatic bottom gate was DC-biased in the range $-50\,\mathrm{V} \le V_g \le 60\,\mathrm{V}$ using a Keithley 2400 source meter. All electrical measurements were carried out in four-probe configuration. In gated measurements, leakage currents were kept below 0.6 nA. The noise floor in the zero-resistance state in Fig. 3i was calculated as the RMS of the voltage in the flat ($I < 3\,\mu\mathrm{A}$) region.

Raman spectroscopy

Raman spectroscopy was carried out using a WITec alpha300 R Raman microscope with a 532 nm laser and 600 g/mm grating. Raman spectra of graphene on SiO_2/Si were normalized by the intensity of the G-peak, at ~1600 cm^{-1}, and graphene spectra of pristine epigraphene on SiC were normalized to the peak at 1714 cm^{-1} which represents the SiC substrate. The spectrum of the SiC substrate was obtained focusing 20 μm down into the substrate on the same spot as the graphene spectrum.

For the detailed Raman analysis of Fig. S3, the 2D- and G-peak positions were extracted from large-area scans of 100 spectra in areas of 27.1×26.8 μm^2 for graphene on SiO_2/Si and 41.6×45.2 μm^2 for as-grown epigraphene using single-Lorentzian fits to 2D- and G-peaks. The shifts of the Raman 2D- and G-peak positions relative to the intrinsic graphene point ($\omega_{G,0}, \omega_{2D,0}$) were decomposed into contributions from mechanical strain and charge transfer (doping) following Lee et al [19].

Selected-area electron diffraction

Selected Area Electron Diffraction (SAED) measurements were performed using a transmission electron microscope (TEM) operated at an acceleration voltage of 300 kV. The electron wavelength (λ) corresponding to this voltage (V) was calculated using the relativistic equation:

$$\lambda = \frac{h}{\sqrt{2m_e eV\left(1+\frac{eV}{2m_e c^2}\right)}} \tag{1}$$

where h is Planck's constant, m_e the free electron mass, and c the speed of light. For 300 kV, the calculated wavelength was 0.0196 Å.

The interplanar spacing d_{hk} was obtained from the SAED pattern using the relation for a 2D hexagonal lattice:

$$d_{hk} = \frac{\lambda L}{R}, \tag{2}$$

where L is the camera length (0.25 m) and R is the measured distance from the central beam to the diffraction spot. R was determined from the SAED image by measuring the distance to the (100) diffraction spot multiple times to obtain an average value, and the measured R_{100} gave $d_{100} = 2.20$ Å.

The lattice constant (a) was calculated from the d-spacing via the relation for a 2D hexagonal lattice:

$$d_{hk} = \frac{a\sqrt{3}}{2\sqrt{h^2+k^2+hk}} \Rightarrow \qquad d_{100} = \frac{a\sqrt{3}}{2} \tag{3}$$

The error was estimated as the standard deviation of multiple R_{100} measurements.

Angle-resolved photoemission spectroscopy

Angle-Resolved Photoemission spectroscopy (ARPES) measurements were carried out in ultra-high vacuum at room temperature. The sample was illuminated by 18.1 eV photons provided by a femtosecond high-harmonic generation (HHG) light source [20].

Field-effect mobility fits

We extracted the field-effect mobility in Fig. 3b and Fig. S6 from a fit of the longitudinal resistivity ρ_{xx} ($B = 0$ T) to a model that accounts for spatial fluctuations in the carrier density (charge puddles) near the Dirac point [21]. Three fitting parameters were used: the mobility μ_{FET}, the carrier density broadening δn, and the residual resistivity ρ_s. The effective carrier density was calculated from the applied gate voltage as

$$n_g = \frac{C_0}{e}(V_g - V_D), \tag{4}$$

where C_0 was taken as the capacitance for a 285 nm SiO_2 gate oxide, $C_0 = 121$ μFm^{-2}.

To account for charge density broadening around charge neutrality, the carrier density was defined as a quadratic function near the Dirac point and otherwise as a linear function [21]:

$$n(V_g) = \begin{cases} \frac{\delta n}{4} + \frac{n_g^2}{\delta n}, & |n_g| \le \delta n/2 \\ |n_g|, & |n_g| > \delta n/2. \end{cases} \tag{5}$$

The carrier density was used in the resistivity expression

$$\rho(V_g) = \frac{1}{e\mu_{FET}\, n(V_g)} + \rho_s \tag{6}$$

and the fitting parameters μ, δn, and ρ_s were determined by fitting the measured ρ_{xx} vs. V_g to Eq. (6).

The density of charged impurities was estimated from the fitted mobility value ($\mu = \mu_{FET}$) as

$$n_{\text{imp}} = (50\, n_0/\mu)\mu_0 \tag{7}$$

with $n_0 = 10^{10}$ cm^{-2} and $\mu_0 = 10^4$ cm^2 V^{-1} s^{-1} [22].

Fits of Hall mobility vs. density

The Hall mobility vs. carrier density in Fig. 3c was obtained via measurements of the longitudinal (ρ_{xx}) and transverse (R_{xy}) resistance components vs. back-gate voltages at constant perpendicular magnetic fields ($B = -1$ T, $B = 0$ T and $B = 1$ T). Data corresponding to the charge puddle regime [23] close to charge neutrality ($n_H = 0$), where $R_{xy}(B)$ is non-linear, were omitted.

At each gate voltage, the Hall coefficient was calculated as

$$R_H = \frac{\mathrm{d}R_{xy}}{\mathrm{d}B}. \tag{8}$$

The carrier densities n_H were calculated as

$$n_H = \frac{1}{R_H e} \tag{9}$$

with e the elementary charge ($e > 0$) such that $n_H < 0$ for holes and $n_H > 0$ for electrons.

The Hall mobilities were calculated as

$$\mu_H = \frac{|R_H|}{\rho_{xx}(B = 0\,\text{T})}. \tag{10}$$

The measured Hall mobility (μ_H) vs. carrier density was fitted to the carrier density (n_H) using a model that combines charged impurity and short-range scattering. Via Matthiessen's rule, the total mean free path is given by:

$$\frac{1}{l_{\text{mfp}}} = \frac{1}{l_{\text{mfp}}^{\text{charge}}} + \frac{1}{l_{\text{mfp}}^{\text{short}}}, \tag{11}$$

with [24]

$$l_{\text{mfp}}^{\text{charge}} \approx A\sqrt{n}, \qquad l_{\text{mfp}}^{\text{short}} \approx \frac{B}{\sqrt{n}}. \tag{12}$$

This yields

$$l_{\text{mfp}} = \frac{AB\sqrt{n}}{B + An}. \tag{13}$$

Using the semiclassical relation for Dirac fermions,

$$\mu = \frac{e\, l_{\text{mfp}}}{\hbar\sqrt{\pi n}}, \tag{14}$$

the mobility becomes

$$\mu_H(n) = \frac{C}{1 + (A/B)n}, \tag{15}$$

where $C = (50\, n_0/n_{\text{imp}})\mu_0$ (C is called μ in Eq. (7)) [22]. This was linearized as:

$$\mu \approx C\left(1 - \frac{A}{B}n\right) \tag{16}$$

for small $(A/B)n$. Using C as a fitting parameter, a fit of the Hall mobility $\mu = \mu_H$ (Eq. (10)) vs. carrier density $n = n_H$ (Eq. (9)) allowed to estimate n_{imp} for the Hall measurements.

Temperature dependence of Shubnikov–de Haas-oscillations

The temperature dependence of the Shubnikov–de Haas (SdH) oscillations in Fig. 3e (ρ_{xx} vs. B) was analyzed within the Lifshitz–Kosevich (LK) formalism [25,26]. The ρ_{xx} vs. B-data at each constant temperature T were normalized as

$$\Delta\rho_{xx}/\rho_{xx,0} = \frac{\rho_{xx} - \rho_{xx}(B = 0\,\text{T})}{\rho_{xx}(B = 0\,\text{T})} \tag{17}$$

and the oscillations were isolated from the $T = 2, 4, 10, 20, 50$ K-data by subtracting a nearly linear (spline) background fitted to the oscillation's center-line; for the 100 K-data a second-order polynomial was subtracted. The SdH oscillation amplitudes A_i were estimated as the $\Delta\rho_{xx}/\rho_{xx,0}$-values at oscillation minima. The uncertainties in A_i – σ_{A_i} – were estimated from the variance across different choices of background subtractions, combined in quadrature with an 8% error consisting of a conservative 5% experimental error and a 3% error for differences in carrier densities at temperatures (because the effective mass depends on the carrier density for Dirac fermions).

For each field B_i corresponding to an oscillation minimum, the amplitudes $A_i(T)$ were fitted in Figure S8a to:

$$A(T, B) = A_0(B)\frac{X}{\sinh X} \tag{18}$$

with X:

$$X = \frac{2\pi^2 k_B T m_e(m_c/m_e)}{\hbar e B}, \tag{19}$$

where k_B is the Boltzmann constant, e the elementary charge, and m_e the free-electron mass, and fitting parameters $A_{0,i}$ and $m_{c,i}/m_e$ (cyclotron mass normalized by free-electron mass).

The uncertainties in m_c/m_e (error bars in Figure S8b) were estimated from fits to the upper and lower amplitude curves defined by $A_i(T) \pm \sigma_{A_i}$:

$$\Delta m_{c,i} = \frac{m_{c,i}^{upper} - m_{c,i}^{lower}}{2}. \tag{20}$$

The mean cyclotron mass was calculated as the arithmetic mean of all fitted values and its uncertainty estimated as the standard deviation of all individual $m_{c,i}/m_e$ values. The prefactor $A_0(B)$ describes the magnetic-field dependent damping due to a finite quantum lifetime τ, and was written as [26]

$$A_0(B) = A_0^* \exp\left(-\frac{\pi}{\omega_c \tau}\right), \tag{21}$$

where the cyclotron frequency is

$$\omega_c = \frac{eB}{m_c}, \tag{22}$$

and the lifetime is related to the Dingle temperature T_D via

$$\tau = \frac{\hbar}{2\pi k_B T_D}. \tag{23}$$

Combining these expressions yields

$$A_0(B) = A_0^* \exp\left[-\frac{2\pi^2 k_B T_D m_c}{e\hbar B}\right] \quad (24)$$

with the logarithmic form

$$\ln A_0(B) = \ln A_0^* - \frac{2\pi^2 k_B T_D m_c}{e\hbar}\frac{1}{B}. \quad (25)$$

A linear fit of $\ln A_0$ vs. $1/B$ (S8c) provides the Dingle temperature T_D from the slope, and the corresponding quantum lifetime from Eq. (23).

The uncertainty in the Dingle temperature T_D was estimated using standard Gaussian error propagation, combining the standard error of the fitted slope of $\ln A_0$ versus $1/B$ with the uncertainty in the effective mass. The uncertainty in the lifetime was obtained by propagating σ_{T_D} through Eq. (23).

Landau index plots

The Landau level index N was assigned to the Shubnikov–de Haas (SdH) oscillation minima in ρ_{xx}. Plotting $1/B_N$ versus N gives a linear relation

$$\frac{1}{B_N} = \frac{4e}{hn_s}\left(N + \tfrac{1}{2}\right), \quad (26)$$

from which the slope yields the carrier density n_s.

Thermodynamic modeling of exfoliation

We use thermodynamic modeling of externally driven transition processes [27] to extract predictions for the probability of selective exfoliation as a function of the characteristic terrace width. The model reflects our picture of selective Si sublimation and graphene-plus-patch formation that is summarized in the main text and developed and further described in Fig. 4f. We treat exfoliation of any given section of graphene as an example of a surface-termination problem where the outcome is dependent on the environment (namely outcomes for other graphene segments) but set by a competition between metastable configurations (see insets of Fig. S14 and [27]). In practice, our predictions emerge after asserting a total-system-energy form (Fig. S15) from DFT inputs (see Supporting Text, DFT-method subsection, and Figs. S12–S14) and setting the ratio of outcome probabilities (for the investigated graphene segment) to a Gibbs-free-energy weighting [27].

Density functional theory

Density functional theory predictions of motifs in the selective Si sublimation, of the strength of Si-C anchor bonds, and (for illustration) of the delamination were done in Quantum Espresso [28], using ultrasoft pseudopotentials with the exchange–correlation approximation set by the strictly parameter-free consistent-exchange vdW-DF-cx [29,30]. We used a slab geometry with a $4 \times 4 \times 3$ repetition of the 4H-SiC unit cell and tracked both surface relaxations and structure changes upon Si atom sublimation.

3. Results and discussion

3.1. Transfer of single-crystalline monolayer graphene

We find that the success in selective one-step delamination and transfer of monolayer graphene from the substrate relies on a specific surface reconstruction – hereafter called a Type A surface – achieved on the silicon-terminated face of 4H-SiC in our growth conditions (see Methods) [18]. During growth, the SiC surface reconstructs, followed by sublimation of silicon atoms (the so-called step-bunching stage), and then the remaining carbon atoms crystallize into a buffer layer with the continuous monolayer graphene atop [8,9]. In our growth process, the surface reconstruction, and consequently the surface morphology, are determined by the growth temperature. In a wide temperature range between $T_0 = 1750$ °C and $T \approx T_0 + 150$ °C, our growth process minimizes step bunching and nearly eliminates multilayer formation. The resulting surface morphology is characterized by narrow terraces and shallow steps, which we identify as hallmarks of the Type A surface. Only large temperature excursions ($T \gtrsim T_0 + 150$ °C) cause another distinct surface reconstruction – hereafter called Type B – which is characterized by wide terraces and higher steps. The Type A surface morphology is key to selective monolayer delamination, whereas the Type B surface reduces the selectivity of the delamination process. Consequently, the temperature stability of the Type A surface allows to significantly relax epigraphene growth optimization to suppress excess graphene patches. The Type A surface is highly reproducible for 7 mm × 7 mm-sized chips in our growth conditions [18]. We have observed selective delamination in over 25 chips, and here we report detailed characterization results from 10 of these.

Fig. 1a illustrates the delamination principle, where epigraphene is covered with an "adhesive layer": a thin metal film ($t > 20$ nm) directly deposited on graphene, with a thermal-release tape for mechanical support (see Methods). Notably, AFM inspection (Fig. 1b) reveals that all excess graphene patches (false-colored), located beneath the topmost graphene layer, remain on the SiC substrate after delaminating the topmost graphene layer from a Type A surface (for a full set of AFM images, see Fig. S1).

To quantitatively characterize the morphology of the Type A surface, Fig. 1c shows histograms of terrace width for Type A epigraphene grown at relaxed temperature conditions, $T_0 + 50$ °C, compared to the surface of Type B epigraphene grown at a higher temperature T_0+150 °C. Type A surfaces exhibit narrow terraces ($w \lesssim 1$ μm), whereas the Type B surfaces exhibit wider terraces with a broader distribution up to $w \lesssim 5$ μm. The corresponding step height histograms (Fig. 1d) reveal shallow steps for the Type A surface, with ~ 75% of the step heights being half a 4H-SiC unit cell (~ 0.5 nm). Type B exhibits higher steps, exceeding 12 4H-SiC-unit cells (~12 nm). Altogether, the Type A surface morphology allows for growth of narrow graphene patches. Indeed, extensive AFM characterization of a Type A SiC surface after graphene delamination reveals that all of the patches found display a width $w < 1.4$ μm (see Fig. S2).

The stark difference between Type A and B surfaces in terms of selective delamination is evident from optical microscope inspection of the transferred graphene layer. Fig. 1e shows a representative graphene monolayer transferred onto SiO_2/Si. This monolayer, derived from a Type A surface, is entirely free of multilayer domains. In contrast, Fig. 1f shows a representative graphene layer transferred from a Type B surface, with excess graphene patches appearing as horizontal dark stripes. These patches co-delaminated with the top graphene layer, an issue reported in earlier work [10,13].

3.2. Surface characterization of transferred graphene

In sharp contrast to earlier reports of graphene delamination from SiC [13] and graphite [31], we find that Type A surfaces enable several metals to selectively delaminate monolayer graphene, with gold in particular resulting in excellent crystalline quality. Fig. 2a shows a comparison of Raman spectra collected for graphene transferred onto SiO_2/Si using gold, silver, and nickel. For reference, the uppermost panel in Fig. 2a shows the characteristic spectral features of epigraphene, namely, a broadened and suppressed 2D-peak [32], and buffer layer bands in the 1350–1570 cm^{-1} range [33]. After gold-assisted transfer to SiO_2/Si, the typical Raman features are similar to those of graphene exfoliated from high-quality graphite crystals [34], with high crystalline quality indicated by absence of the defect-induced D-peak (~1350 cm^{-1}), and a sharp, symmetric 2D-peak with full-width at half-maximum (FWHM) 28 cm^{-1}. Fig. 2a further shows that silver and nickel, which also enable highly selective monolayer delamination (later demonstrated in Figs. 3h and S11), result in defected graphene, as indicated by a noticeable D-peak (most pronounced in the case of nickel). Additionally, we note that all graphene Raman peaks red-shift after transferring graphene from SiC to SiO_2/Si, likely due to the release

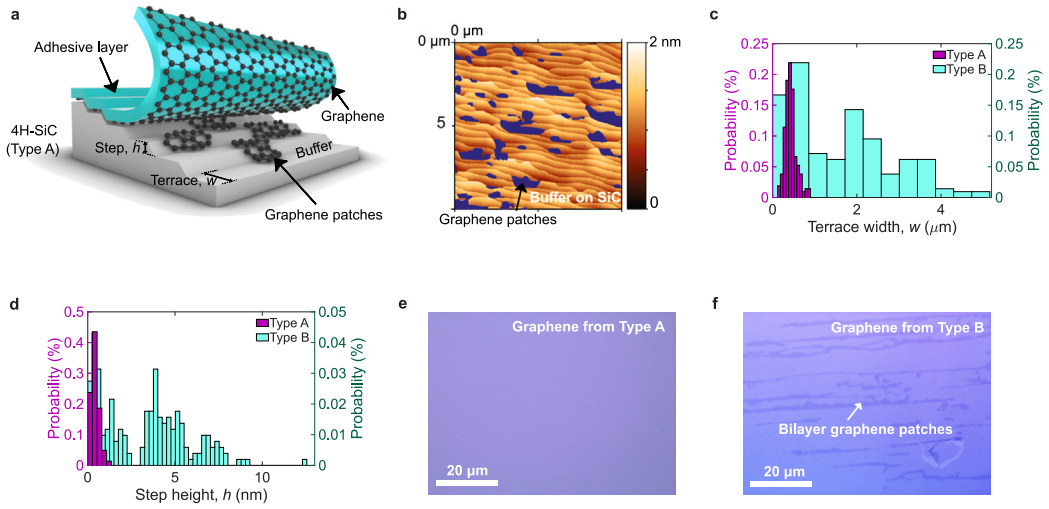

Fig. 1. Production of single-crystalline monolayer graphene. (a) Illustration of delamination of epigraphene from a Type A SiC surface, where excess graphene patches are left behind on the substrate, i.e. on the buffer layer. (b) AFM topography map of the Type A SiC substrate after graphene delamination, where all the excess graphene patches remain after delamination; these are overlaid in false color (blue). (c) Terrace width histogram obtained from AFM data, normalized to probability, for Type A and B SiC surface reconstructions. (d) Same as (c) for step height. (e) Optical micrograph of epigraphene delaminated from a Type A SiC substrate and transferred to SiO_2/Si. Note the absence of graphene patches. (f) Same as (e) with graphene delaminated from a Type B surface, where bilayer patches co-delaminated with the top graphene layer.

of compressive strain upon delamination from the SiC substrate [32]. A more detailed Raman analysis [19] (see Fig. S3) indicates compressive strain for epigraphene, and tensile strain and p-doping for graphene on SiO_2/Si. Fig. 2b shows a selected-area electron diffraction (SAED) pattern of graphene delaminated from SiC and transferred onto an amorphous carbon-TEM grid, showing diffraction spots of graphene with lattice parameter $a = 2.54 \pm 0.02$ Å (see Methods), higher than the theoretical value ($a = 2.46$ Å), indicating a graphene lattice under tensile strain.

The linear Dirac dispersion of the transferred graphene is confirmed by ARPES measurements performed with $E = 18.1$ eV photons and spot size ~100 µm [20]. Fig. 2c shows the typical band structure of as-grown epigraphene, with the Fermi level (E_F) positioned 400 meV above the Dirac point, consistent with other reports on epigraphene [36]. This corresponds to an electron density $n = \frac{1}{\pi}\left(\frac{E_F}{\hbar v_F}\right)^2 \approx 7.0 \times 10^{12}$ cm^{-2} with the Fermi velocity $v_F = 1.3 \times 10^6$ ms^{-1} extracted from the fit of the ARPES peak intensity positions (see Supporting Text). After Au-assisted transfer onto SiO_2/Si (Fig. 2d), graphene turns p-doped due to interaction with the oxide. Interestingly, the Fermi velocity of carriers nearly doubles to $v_F = 2.2 \times 10^6$ ms^{-1}, approaching values reported for suspended graphene [37]. This increase, along with the momentum broadening $\Delta k_{\parallel} = 0.11$Å^{-1}, small for graphene on a SiO_2/Si substrate, is a consequence of high crystallinity and reduced electron–electron screening in the local dielectric environment [38]. We note that the suppressed photoemission intensity of the Dirac state at positive momenta in Fig. 2d arises from the experimental geometry, and the right-branch dispersion remains traceable at higher binding energies (see Fig. S4). Altogether, the combined electron diffraction, Raman, and ARPES analyses demonstrate that the crystalline quality of graphene is retained after delamination and transfer from the SiC substrate.

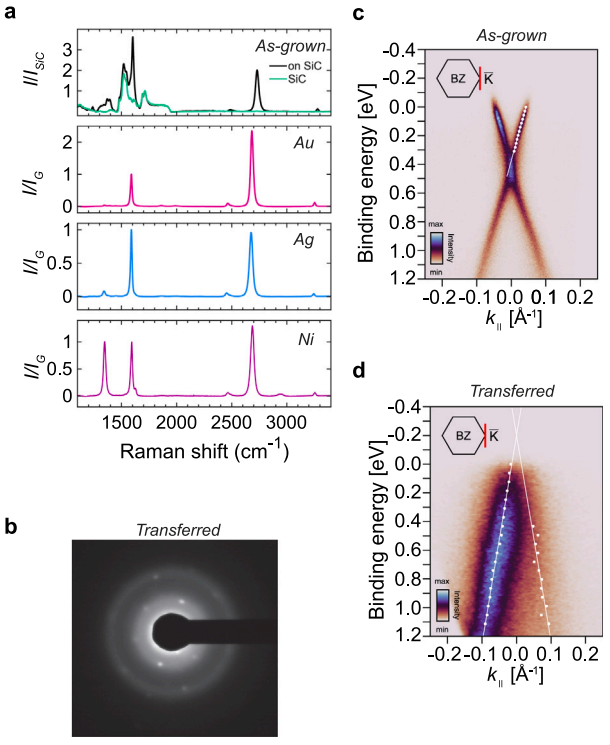

Fig. 2. Surface characterization of graphene delaminated from SiC. (a) Raman spectra (532 nm laser) for as-grown epigraphene on SiC (black line) along with the 4H-SiC substrate underneath the graphene (green line), and graphene transferred from SiC to SiO_2/Si using different metals (gold, silver, and nickel). (b) SAED pattern of graphene transferred from SiC onto a holey carbon TEM grid. The hexagonal spot array represents graphene with lattice parameter $a = 2.54 \pm 0.02$ Å. The diffuse halo is characteristic of amorphous carbon of the TEM grid. (c) ARPES band structure for as-grown graphene on SiC represented as an energy–momentum cut through the $\bar{K}$-point in the Brillouin zone as indicated in the inset. The dotted line is a linear fit to the band dispersion close to the Fermi level used to extract the Fermi velocity. (d) Same as (c) for graphene transferred to SiO_2/Si. As a consequence of the polarization of the light, only one branch of the band structure is visible [35].

3.3. Electrical transport of transferred graphene

Magneto-transport measurements reveal that epigraphene transferred onto SiO_2/Si exhibits transport properties that are indistinguishable from those of high-quality exfoliated graphene flakes on the same substrate. Fig. 3a shows a typical Hall bar device on SiO_2/Si produced by gold-assisted delamination. To protect graphene from the ambient, devices were passivated with PMMA resist before measurements of the longitudinal resistivity, ρ_{xx} (= $R_{xx}W/L$), and transverse resistance,

R_{xy}. Fits of ρ_{xx} to the field-effect response [21] in Fig. 3b (using Eq. (6)) yield a carrier mobility $\mu_{FET} = 8670$ cm^2 V^{-1} s^{-1} at 300 K, in agreement with those extracted from low-field ($|B| < 1$ T) Hall effect measurements. The Hall mobilities ($\mu_H = |R_H|/\rho_{xx}(B = 0\,\mathrm{T})$) exhibit only a weak linear decrease with carrier density ($n_H = \frac{1}{eR_H}$) in the range $n_H \approx 1$–4×10^{12} cm^{-2}, as shown in Fig. 3c. The carrier mobility is limited by charged impurity scattering, typical of graphene on SiO_2/Si [22,39], with a charged impurity density $n_{\mathrm{imp}} \sim 5-6\times10^{11}$ cm^{-2} obtained from fits to μ_{FET} and μ_H (see Tables S1–S2). The values of room-temperature carrier mobilities are high considering substrate-scattering effects, metal residues (see S5) and the polymer encapsulating layer. At low temperatures, these limit the mobility values to $\mu_{FET} = 11{,}000$ cm^2 V^{-1} s^{-1} and $\mu_H = 12{,}500$ cm^2 V^{-1} s^{-1} at $T = 2$ K. Altogether, the observed room-temperature carrier mobilities in transferred graphene approach the upper limit for graphene on SiO_2/Si substrates [40], and exceed typical mobilities reported for epigraphene, which are in the 1000 cm^2 V^{-1} s^{-1}-range [41].

The observation of the half-integer quantum Hall effect (QHE) gives unequivocal evidence that all electronic properties of graphene are preserved after transfer from SiC [42,43]. Fig. 3d presents the gate response of ρ_{xx} and R_{xy}, measured at $T = 2$ K and $B = 14$ T, which shows quantum Hall plateaus in R_{xy} and vanishing ρ_{xx} at filling factors $|\nu| = 2, 6, 10$ ($\nu = 4N + 2$ with Landau index N) [43]. The observation of QH plateaus for filling factors $|\nu| > 2$ is noteworthy because they are difficult to observe for epigraphene due to disorder (intervalley scattering) caused by the stepped SiC substrate [44]. This indicates that the corrugation of epigraphene due to the steps in SiC and the concomitant interaction with the buffer layer [45] is not inherited by the transferred material (this is also supported by AFM data in Fig. S5).

Higher-order Landau levels up to filling factor $\nu = 74$ are also observable in the magnetoresistance of the transferred graphene device. Fig. 3e shows Shubnikov–de Haas (SdH)-oscillations for electrons in the metallic limit ($n_H \approx 3.8 \times 10^{12}$ cm^{-2}) at different temperatures, persisting up to $T = 150$ K. At large N, Landau levels are closely spaced in energy, so their manifestation as quantum oscillations in ρ_{xx} requires a small disorder-induced energy broadening. To quantify the energy broadening, we analyzed the temperature- and field-dependence of the oscillation amplitudes within the Lifshitz–Kosevich formalism (see Methods and Fig. S8) [25,26]. From this, we estimate the cyclotron mass to $m_c/m_e = 0.044 \pm 0.0056$ with m_e the free-electron mass, lifetime $\tau = 50.8 \pm 6.59$ fs, and Dingle temperature $T_D = 23.9 \pm 3.10$ K, with the errors given as the expanded uncertainty with coverage factor $k = 1$. These are typical values for exfoliated graphene on SiO_2/Si at similar carrier densities [26,42]. Fig. 3f shows a plot of $\frac{1}{B_N}$ versus N, where B_N denotes the magnetic field strength corresponding to Landau index N at an SdH-oscillation minimum in ρ_{xx} at $T = 2$ K (see full data in Fig. S7). A linear fit yields carrier densities n_s (Eq. (26)) in agreement with those from linear Hall slopes (n_H). Extrapolating to $1/B_N = 0$ yields the intercept $N \approx -\frac{1}{2}$ reflecting the Berry phase of π in monolayer graphene [42,43].

We use quantum transport to verify the single-crystallinity of our large-area graphene, through the demonstration of the half-integer quantum Hall effect in near-centimeter-sized devices. A zero-resistance state ($\rho_{xx} = 0$) has been difficult to achieve in graphene produced by any other method, notably CVD graphene, due to grain boundaries [16,46,47], or even epigraphene due to bilayer patches [14,17]. Yet, graphene transferred from SiC allows for $\rho_{xx} = 0$ even when silver, known to give slightly defective graphene (see Fig. 2a), is used as the delamination layer. Fig. 3g shows a 7 mm × 7 mm SiO_2/Si substrate covered with silver-assisted transferred graphene, fitted with electrical contacts by shadow mask deposition. Room-temperature mobilities extracted from van der Pauw measurements are of the order of 1000 cm^2 V^{-1} s^{-1} (see Fig. S6). At low temperatures, the gate voltage response of ρ_{xx} and R_{xy} (Fig. 3h) exhibits QH plateaus for filling factors $|\nu| = 2, 6, 10, 14$. We verified the zero-resistance state by measuring the current–voltage (I–V) curves at the $\nu = \pm2$-plateaus across diagonal contacts V_{xy}^+ and V_{xy}^-. Fig. 3i shows the I–V curve in logarithmic scale (see plot in linear scale in Fig. S9) that confirms the non-dissipative state for both holes and electrons, limited by the noise floor of $V_{rms} = 83$ nV. The voltage signal increases exponentially for currents above a critical value ($I_c \approx 3$ μA), indicating breakdown of the QHE. Significantly, the zero-resistance state provides evidence for the absence of grain boundaries or major doping or structural inhomogeneities across the entire graphene area, because these would short QH edge currents and result in a finite longitudinal resistance [16,46].

3.4. Wafer-scale graphene transfer

We demonstrate the scalability of our process through the delamination and transfer of epigraphene grown on recycled 4"-SiC wafers (see Methods), shown in Fig. 4a. Epigraphene growth on recycled wafers results in a predominantly Type B surface morphology where up to 40% of the area contains excess graphene (see Fig. 4b). The transferred graphene, in contrast, exhibits a remarkably low bilayer content. We quantified this by optical mapping of graphene transferred onto SiO_2/Si substrate (Fig. 4c) via the optical contrast difference between mono- and bilayer graphene [14]. In total, we sampled 300 microscope images on the 4"-wafer, each corresponding to an area of 290 × 190 μm^2. An example with 1% bilayer content is shown in Fig. 4d, and the result of the wafer mapping is shown in Fig. 4e (color map) and Figure S10 (histograms). The median value of the bilayer graphene content of the transferred graphene is 4.3%, implying a ~10-fold reduction of excess graphene layers with respect to the as-grown material using our delamination method.

3.5. Type A epigraphene

Our experiments also provide an alternative perspective on epigraphene growth and the significance of SiC surface morphology for producing patch-free graphene. In addition to gold and silver as described earlier, we find that nickel – reported to delaminate graphene multilayers from SiC and graphite [10,13,31] – leads to highly selective monolayer delamination from a Type A substrate (see Fig. S11). To interpret these results, we introduce a thermodynamic exfoliation model, where we use (i) free-energy differences to predict surface termination and structure [27] and (ii) density functional theory (DFT) to model Si sublimation by tracking surface relaxations [27,28]. We compute parameters for a total-system-energy descriptor using van der Waals (vdW)-inclusive DFT [28–30] (see Methods, Supporting Information and Figs. S12–S15). The Type A epigraphene in our model is illustrated in Fig. 4f: SiC terraces are covered with a buffer layer, patches are anchored to the substrate by chemical bonds to Si atoms at the step edges, and the top graphene layer extends over the whole substrate. The vdW attraction between graphene and the patch is slightly stronger than that between the patch and buffer, but weaker than the Si–C anchoring per carbon atom involved. Hence, our model predicts that wide patches are likely to co-delaminate with the top graphene layer, because as its width increases, the net impact by vdW forces outweighs the Si–C anchoring (see Fig. S15). This gives an interpretation why a Type A surface (with its narrow patches) enables selective monolayer delamination.

4. Conclusion

In summary, we have shown that the ability to produce single-crystalline graphene, free from graphene multilayers and grain boundaries, stems from our capability to achieve a specific (Type A) surface reconstruction of 4H-SiC. We transferred the graphene monolayer from the SiC substrate without compromising its crystalline quality, resulting in high carrier mobilities and preservation of all graphene-specific quantum transport features. Furthermore, by extending our process to

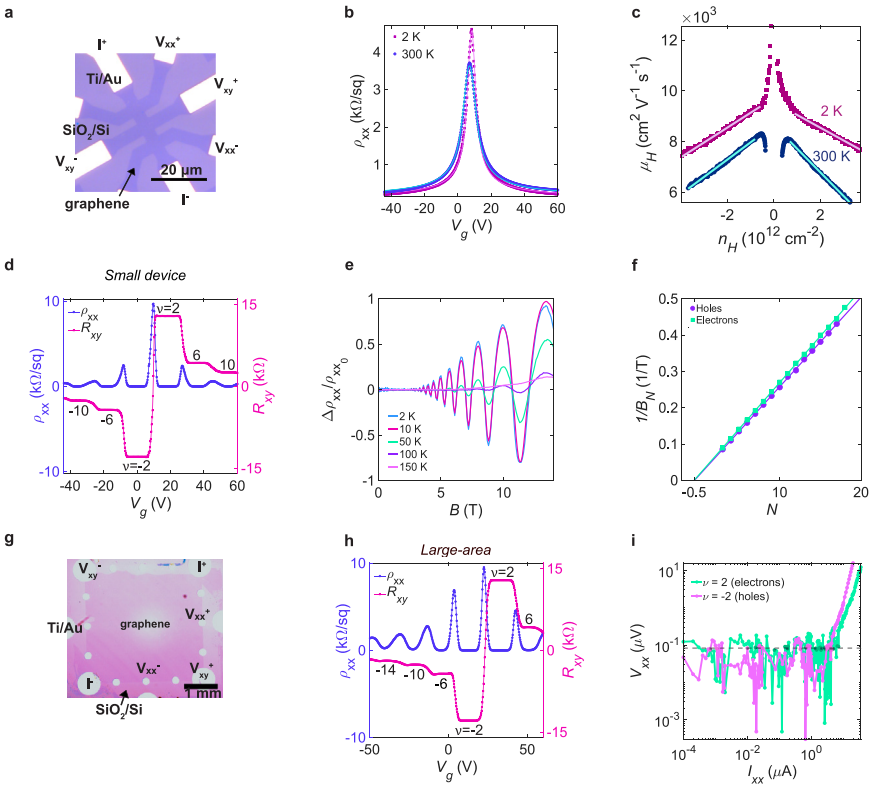

Fig. 3. Electrical transport in graphene transferred from SiC onto SiO_2/Si. (a) Hall bar with gold-transferred graphene ($W = 5\,\mu m$, $L = 15\,\mu m$) and passivated with PMMA. (b) Sheet resistivity vs. gate voltage at $T = 300$ K (blue dots) and $T = 2$ K (purple squares); solid lines are FET mobility fits. (c) Hall mobilities vs. carrier densities at $T = 300$ K (blue dots) and $T = 2$ K (magenta squares). Solid lines are fits to Eq. (16). (d) Half-integer QHE at $B = 14$ T and $T = 2$ K showing $\nu = 2, 6, 10$. (e) Temperature dependence of SdH-oscillations for electrons ($V_g = 60$ V; $n = 3.8 \times 10^{12}$ cm^{-2}). (f) Landau index plot from SdH ρ_{xx} minima at 2 K for holes ($V_g = -44$ V) and electrons ($V_g = 60$ V). (g) Large-area device with silver-transferred graphene on SiO_2/Si. (h) Half-integer QHE at $B = 14$ T, $T = 2$ K in the large-area device. (i) Zero-resistance state ($\rho_{xx} = 0$) in I–V curves measured at the $\nu = \pm 2$-plateaus ($B = 14$ T) for electrons ($V_g = 35$ V) and holes ($V_g = 15$ V) for $I_{xx} > 0$. The dashed line indicates the noise floor ($V_{rms} = 83$ nV).

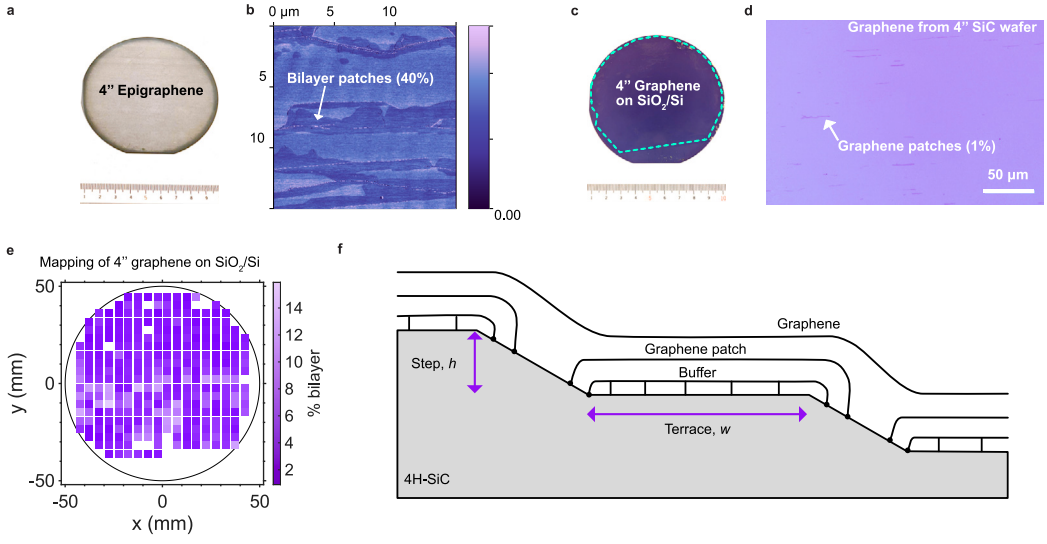

Fig. 4. Delamination and transfer of wafer-scale epigraphene. (a) As-grown epigraphene on a recycled 4'' SiC wafer. (b) A representative $15 \times 15\ \mu m^2$ AFM phase map of epigraphene grown on a 4''-SiC wafer, showing the presence of bilayer domains (dark) that cover 40% of the total area. (c) 4''-sized graphene transferred from SiC to a 4''-SiO_2/Si wafer. (d) Optical micrograph of graphene transferred from the 4''-SiC wafer to SiO_2/Si, showing the presence of bilayer domains (dark stripes) on monolayer graphene that cover 1% of the area. (e) Mapping of the percentage of bilayer graphene over the SiO_2/Si wafer (see panel c) with a median value of 4.3%. Each square corresponds to an area of $290 \times 190\ \mu m^2$; the white regions correspond to areas with no graphene. (f) Schematic illustration of epigraphene on SiC within our growth model. The black circles represent anchor points of graphene patches or the buffer layer to the substrate.

recycled wafers, we demonstrate that the high cost associated with the SiC substrate [48] can be circumvented. Our results thereby establish SiC as an attractive generic platform – alternative to CVD on metal catalysts – for the mass production of single-crystalline graphene needed in high-performance applications.

CRediT authorship contribution statement

Johanna Udén: Writing – original draft, Writing – review & editing, Resources, Methodology, Investigation, Formal analysis, Data curation, Conceptualization. **Joyal Jain Palakulam:** Writing – review & editing, Resources, Methodology, Investigation, Formal analysis, Data curation. **Awse Salha:** Writing – review & editing, Resources, Investigation. **Per Hyldgaard:** Writing – review & editing, Writing – original draft, Resources, Methodology, Investigation, Funding acquisition, Formal analysis. **Elsebeth Schröder:** Writing – review & editing, Writing – original draft, Resources, Methodology, Investigation, Funding acquisition, Formal analysis. **Magnus Hårdensson Berntsen:** Writing – review & editing, Writing – original draft, Resources, Methodology, Investigation, Formal analysis, Data curation. **Maciej Dendzik:** Resources, Methodology, Investigation, Formal analysis, Data curation. **Wanyu Chen:** Resources, Methodology, Investigation, Formal analysis, Data curation. **Oscar Tjernberg:** Writing – review & editing, Resources, Methodology, Investigation, Funding acquisition, Formal analysis, Data curation. **Manasi Shah:** Writing – review & editing, Resources, Methodology, Investigation, Formal analysis, Data curation. **Rodrigo Martinez-Duarte:** Writing – review & editing, Resources, Methodology, Investigation, Funding acquisition, Formal analysis, Data curation. **Hans He:** Writing – review & editing, Investigation, Funding acquisition, Formal analysis. **Johannes Hofmann:** Writing – review & editing, Supervision, Funding acquisition, Formal analysis. **Thilo Bauch:** Writing – review & editing, Supervision, Funding acquisition, Formal analysis. **Naveen Shetty:** Writing – review & editing, Supervision, Resources, Methodology, Investigation, Formal analysis, Data curation. **Samuel Lara-Avila:** Writing – review & editing, Writing – original draft, Supervision, Resources, Methodology, Investigation, Funding acquisition, Formal analysis, Conceptualization.

Declaration of competing interest

The authors declare that they have no known competing financial interests or personal relationships that could have appeared to influence the work reported in this paper.

Acknowledgments

This work was jointly supported by Chalmers Area of Advance Nano, Chalmers Area of Advance Materials, 2D-Tech VINNOVA competence Center (Ref. [2024-03852]), and the Swedish Research Council VR under Contract No. 2021-05252 (J.U., S.L.A, N.S., J.J.P.), VR Contract No. 2022-03277 (P.H.), VR Contract No. 2020-04997 (E.S.), Knut and Alice Wallenberg Foundation No. 2018-0104 (O.T, M.D., W.C., M.H.B.), US National Science Foundation (NSF) award No. 2412500 (R.M.-D., M.S.), VINNOVA 2023-03438 (H.H.), and VR Grant No. 2024-04485, Olle Engkvist Grant No. 233-0339, Nordita and KAW No. 2024.0129 (J.H.). Computer resources were supported by Chalmers C3SE and the National Academic Infrastructure for Supercomputing in Sweden under contracts NAISS2024/3-16 and NAISS2024-6-432 (E.S., P.H.). This work was performed in part at Myfab Chalmers and Chalmers Materials Analysis Laboratory (CMAL). We gratefully acknowledge Prof. Rositsa Yakimova and Prof. August Yurgens for insightful discussions.

Appendix A. Supplementary data

Supplementary material related to this article can be found online at https://doi.org/10.1016/j.carbon.2026.121963.

References

[1] Y. Zhao, L. Lin, Graphene and beyond lab benches, Science 386 (2024) 144–146, http://dx.doi.org/10.1126/science.ads4149.
[2] R. Ma, Q. Huan, L. Wu, J. Yan, W. Guo, Y.Y. Zhang, S. Wang, L. Bao, Y. Liu, S. Du, S.T. Pantelides, H.J. Gao, Direct four-probe measurement of grain-boundary resistivity and mobility in millimeter-sized graphene, Nano Lett. 17 (2017) 5291–5296, http://dx.doi.org/10.1021/acs.nanolett.7b01624.
[3] J. Zhang, J. Zhao, J. Lu, Intrinsic strength and failure behaviors of graphene grain boundaries, ACS Nano 6 (2012) 2704–2711, http://dx.doi.org/10.1021/nn3001356.
[4] P. Yasaei, B. Kumar, R. Hantehzadeh, M. Kayyalha, A. Baskin, N. Repnin, C. Wang, R.F. Klie, Y.P. Chen, P. Král, A. Salehi-Khojin, Chemical sensing with switchable transport channels in graphene grain boundaries, Nat. Commun. 5 (2014) http://dx.doi.org/10.1038/ncomms5911.
[5] Bárbara Canto, Martin Otto, Arantxa Maestre, Alba Centeno, Amaia Zurutuza, Bianca Robertz, Eros Reato, Bartos Chmielak, Stefanie L. Stoll, Andreas Hemmetter, Florian Schlachter, Lisa Ehlert, Sha Li, Daniel Neumaier, Gordon Rinke, Zhenxing Wang, Max C. Lemme, Multi-project wafer runs for electronic graphene devices in the European 2D-Experimental Pilot Line project, Nat. Commun. 16 (2025) http://dx.doi.org/10.1038/s41467-025-56357-0.
[6] M. Wang, M. Huang, D. Luo, Y. Li, M. Choe, W.K. Seong, M. Kim, S. Jin, M. Wang, S. Chatterjee, Y. Kwon, Z. Lee, R.S. Ruoff, Single-crystal, large-area, fold-free monolayer graphene, Nature 596 (2021) 519–524, http://dx.doi.org/10.1038/s41586-021-03753-3.
[7] J. Amontree, X. Yan, C.S. DiMarco, P.L. Levesque, T. Adel, J. Pack, M. Holbrook, C. Cupo, Z. Wang, D. Sun, A.J. Biacchi, C.E. Wilson-Stokes, K. Watanabe, T. Taniguchi, C.R. Dean, A.R. Hight Walker, K. Barmak, R. Martel, J. Hone, Reproducible graphene synthesis by oxygen-free chemical vapour deposition, Nature 630 (2024) 636–642, http://dx.doi.org/10.1038/s41586-024-07454-5.
[8] W. Norimatsu, M. Kusunoki, Epitaxial graphene on SiC{0001}: Advances and perspectives, Phys. Chem. Chem. Phys. 16 (2014) 3501–3511, http://dx.doi.org/10.1039/c3cp54523g.
[9] G.R. Yazdi, T. Iakimov, R. Yakimova, Epitaxial graphene on SiC: A review of growth and characterization, Crystals 6 (2016) http://dx.doi.org/10.3390/cryst6050053.
[10] S.H. Bae, X. Zhou, S. Kim, Y.S. Lee, S.S. Cruz, Y. Kim, J.B. Hannon, Y. Yang, D.K. Sadana, F.M. Ross, H. Park, J. Kim, Unveiling the carrier transport mechanism in epitaxial graphene for forming wafer-scale, single-domain graphene, Proc. Natl. Acad. Sci. USA 114 (2017) 4082–4086, http://dx.doi.org/10.1073/pnas.1620176114.
[11] S. Unarunotai, Y. Murata, C.E. Chialvo, H.S. Kim, S. MacLaren, N. Mason, I. Petrov, J.A. Rogers, Transfer of graphene layers grown on SiC wafers to other substrates and their integration into field effect transistors, Appl. Phys. Lett. 95 (2009) http://dx.doi.org/10.1063/1.3263942.
[12] S. Unarunotai, J.C. Koepke, C.L. Tsai, F. Du, C.E. Chialvo, Y. Murata, R. Haasch, I. Petrov, N. Mason, M. Shim, J. Lyding, J.A. Rogers, Layer-by-layer transfer of multiple, large area sheets of graphene grown in multilayer stacks on a single SiC wafer, ACS Nano 4 (2010) 5591–5598, http://dx.doi.org/10.1021/nn101896a.
[13] J. Kim, H. Park, J.B. Hannon, S.W. Bedell, K. Fogel, D.K. Sadana, C. Dimitrakopoulos, Layer-resolved graphene transfer via engineered strain layers, Science 342 (2013) 830–833, http://dx.doi.org/10.1126/science.1242988.
[14] T. Yager, A. Lartsev, S. Mahashabde, S. Charpentier, D. Davidovikj, A. Danilov, R. Yakimova, V. Panchal, O. Kazakova, A. Tzalenchuk, S. Lara-Avila, S. Kubatkin, Express optical analysis of epitaxial graphene on SiC: Impact of morphology on quantum transport, Nano Lett. 13 (2013) 4217–4223, http://dx.doi.org/10.1021/nl402347g.
[15] Y. Cao, V. Fatemi, S. Fang, K. Watanabe, T. Taniguchi, E. Kaxiras, P. Jarillo-Herrero, Unconventional superconductivity in magic-angle graphene superlattices, Nature 556 (2018) 43–50.
[16] A.W. Cummings, A. Cresti, S. Roche, Quantum Hall effect in polycrystalline graphene: The role of grain boundaries, Phys. Rev. B 90 (2014) http://dx.doi.org/10.1103/PhysRevB.90.161401.
[17] A. Bergvall, J.M. Carlsson, T. Löfwander, Influence of [0001] tilt grain boundaries on the destruction of the quantum Hall effect in graphene, Phys. Rev. B 91 (2015) http://dx.doi.org/10.1103/PhysRevB.91.245425.
[18] N. Shetty, F. Chianese, H. He, J. Huhtasaari, S. Ghasemi, K. Moth-Poulsen, S. Kubatkin, T. Bauch, S. Lara-Avila, Ultralow 1/f noise in epigraphene devices, Appl. Phys. Lett. 124 (2024) http://dx.doi.org/10.1063/5.0185890.
[19] J.E. Lee, G. Ahn, J. Shim, Y.S. Lee, S. Ryu, Optical separation of mechanical strain from charge doping in graphene, Nat. Commun. 3 (2012) http://dx.doi.org/10.1038/ncomms2022.
[20] Q. Guo, M. Dendzik, A. Grubišić-Cabo, M.H. Berntsen, C. Li, W. Chen, B. Matta, U. Starke, B. Hessmo, J. Weissenrieder, O. Tjernberg, A narrow bandwidth extreme ultra-violet light source for time- and angle-resolved photoemission spectroscopy, Struct. Dyn. 9 (2022) http://dx.doi.org/10.1063/4.0000149.
[21] J.H. Gosling, O. Makarovsky, F. Wang, N.D. Cottam, M.T. Greenaway, A. Patanè, R.D. Wildman, C.J. Tuck, L. Turyanska, T.M. Fromhold, Universal mobility characteristics of graphene originating from charge scattering by ionised impurities, Commun. Phys. 4 (2021) http://dx.doi.org/10.1038/s42005-021-00518-2.

[22] S. Adam, E.H. Hwang, V.M. Galitski, S. Das Sarma, A self-consistent theory for graphene transport, Proc. Natl. Acad. Sci. 104 (2007) 18392–18397, http://dx.doi.org/10.1073/pnas.0704772104.
[23] Yuanbo Zhang, Victor W. Brar, Caglar Girit, Alex Zettl, Michael F. Crommie, Origin of spatial charge inhomogeneity in graphene, Nat. Phys. 5 (2009) 722–726, http://dx.doi.org/10.1038/nphys1365.
[24] Kentaro Nomura, A.H. MacDonald, Quantum transport of massless Dirac fermions, Phys. Rev. Lett. 98 (7) (2007) http://dx.doi.org/10.1103/PhysRevLett.98.076602.
[25] T. Ando, A.B. Fowler, F. Stern, Electronic properties of two-dimensional systems, Rev. Modern Phys. 54 (1982) http://dx.doi.org/10.1103/RevModPhys.54.437.
[26] Z. Tan, C. Tan, L. Ma, G.T. Liu, L. Lu, C.L. Yang, Shubnikov-de Haas oscillations of a single layer graphene under dc current bias, Phys. Rev. B 84 (2011) http://dx.doi.org/10.1103/PhysRevB.84.115429.
[27] Jochen Rohrer, Per Hyldgaard, Ab initio thermodynamics of deposition growth: Surface terminations of TiC(111) and TiN(111) grown by chemical vapor deposition, Phys. Rev. B - Condens. Matter Mater. Phys. 82 (4) (2010) http://dx.doi.org/10.1103/PhysRevB.82.045415.
[28] P. Giannozzi, et al., Advanced capabilities for materials modelling with Quantum ESPRESSO, J. Phys. Condens. Matter 29 (46) (2017) http://dx.doi.org/10.1088/1361-648X/aa8f79.
[29] M. Dion, H. Rydberg, E. Schröder, D.C. Langreth, B.I. Lundqvist, Van der waals density functional for general geometries, Phys. Rev. Lett. 92 (24) (2004) http://dx.doi.org/10.1103/PhysRevLett.92.246401.
[30] Per Hyldgaard, Yang Jiao, Vivekanand Shukla, Screening nature of the van der Waals density functional method: A review and analysis of the many-body physics foundation, J. Phys. Condens. Matter 32 (39) (2020) http://dx.doi.org/10.1088/1361-648X/ab8250.
[31] J.-Y. Moon, M. Kim, S.-I. Kim, S. Xu, J.-H. Choi, D. Whang, K. Watanabe, T. Taniguchi, D.S. Park, J. Seo, S.-H. Cho, S.-K. Son, J.-H. Lee, Layer-engineered large-area exfoliation of graphene, Sci. Adv. 6 (2020).
[32] J. Röhrl, M. Hundhausen, K.V. Emtsev, Th. Seyller, R. Graupner, L. Ley, Raman spectra of epitaxial graphene on SiC(0001), Appl. Phys. Lett. 92 (2008) http://dx.doi.org/10.1063/1.2929746.
[33] T. Milenov, P. Rafailov, R. Yakimova, I. Shtepliuk, V. Popov, Raman fingerprint of the graphene buffer layer grown on the Si-terminated face of 4H-SiC(0001): Experiment and theory, J. Raman Spectrosc. 55 (2024) 416–424, http://dx.doi.org/10.1002/jrs.6642.
[34] A.C. Ferrari, D.M. Basko, Raman spectroscopy as a versatile tool for studying the properties of graphene, Nature Nanotechnology 8 (2013) 235–246, http://dx.doi.org/10.1038/nnano.2013.46.
[35] Isabella Gierz, Jürgen Henk, Hartmut Höchst, Christian R. Ast, Klaus Kern, Illuminating the dark corridor in graphene: Polarization dependence of angle-resolved photoemission spectroscopy on graphene, Phys. Rev. B - Condens. Matter Mater. Phys. 83 (12) (2011) http://dx.doi.org/10.1103/PhysRevB.83.121408.
[36] U. Starke, C. Riedl, Epitaxial graphene on SiC(0001) and SiC(000-1): From surface reconstructions to carbon electronics, J. Phys.: Condens. Matter. 21 (2009) http://dx.doi.org/10.1088/0953-8984/21/13/134016.
[37] D.C. Elias, R.V. Gorbachev, A.S. Mayorov, S.V. Morozov, A.A. Zhukov, P. Blake, L.A. Ponomarenko, I.V. Grigorieva, K.S. Novoselov, F. Guinea, A.K. Geim, Dirac cones reshaped by interaction effects in suspended graphene, Nat. Phys. 7 (2011) 701–704, http://dx.doi.org/10.1038/nphys2049.
[38] C. Hwang, D.A. Siegel, S.K. Mo, W. Regan, A. Ismach, Y. Zhang, A. Zettl, A. Lanzara, Fermi velocity engineering in graphene by substrate modification, Sci. Rep. 2 (2012) http://dx.doi.org/10.1038/srep00590.
[39] J.H. Chen, C. Jang, S. Adam, M.S. Fuhrer, E.D. Williams, M. Ishigami, Charged-impurity scattering in graphene, Nat. Phys. 4 (2008) 377–381, http://dx.doi.org/10.1038/nphys935.
[40] A. Tyagi, V. Mišeikis, L. Martini, S. Forti, N. Mishra, Z.M. Gebeyehu, M.A. Giambra, J. Zribi, D. Aureau M. Frégnaux, M. Romagnoli, F. Beltram, C. Coletti, Ultra-clean high-mobility graphene on technologically relevant substrates, Nanoscale 14 (2022) 2167–2176, http://dx.doi.org/10.1039/d1nr05904a.
[41] W. Norimatsu, A review on carrier mobilities of epitaxial graphene on silicon carbide, Materials 16 (2023) http://dx.doi.org/10.3390/ma16247668.
[42] K.S. Novoselov, A.K. Geim, S.V. Morozov, D. Jiang, M.I. Katsnelson, I.V. Grigorieva, S.V. Dubonos, A.A. Firsov, Two-dimensional gas of massless Dirac fermions in graphene, Nature 438 (2005) 197–200, http://dx.doi.org/10.1038/nature04233.
[43] Yuanbo Zhang, Yan Wen Tan, Horst L. Stormer, Philip Kim, Experimental observation of the quantum hall effect and Berry's phase in graphene, Nature 438 (7065) (2005) 201–204, http://dx.doi.org/10.1038/nature04235.
[44] S. Lara-Avila, A. Tzalenchuk, S. Kubatkin, R. Yakimova, T.J.B.M. Janssen, K. Cedergren, T. Bergsten, V. Fal'ko, Disordered Fermi liquid in epitaxial graphene from quantum transport measurements, Phys. Rev. Lett. 107 (2011) http://dx.doi.org/10.1103/PhysRevLett.107.166602.
[45] T.A. De Jong, L. Visser, J. Jobst, R.M. Tromp, S.J. van der Molen, Stacking domain morphology in epitaxial graphene on silicon carbide, Phys. Rev. Mater. 7 (2023) http://dx.doi.org/10.1103/PhysRevMaterials.7.034001.
[46] F. Lafont, R. Ribeiro-Palau, Z. Han, A. Cresti, A. Delvallée, A.W. Cummings, S. Roche, V. Bouchiat, S. Ducourtieux, F. Schopfer, W. Poirier, Anomalous dissipation mechanism and Hall quantization limit in polycrystalline graphene grown by chemical vapor deposition, Phys. Rev. B 90 (2014) http://dx.doi.org/10.1103/PhysRevB.90.115422.
[47] T.K. Chau, D. Suh, H. Kang, Quantum Hall effect across graphene grain boundary, Materials 15 (2022) http://dx.doi.org/10.3390/ma15010008.
[48] Rickard Arvidsson, Sverker Molander, Prospective life cycle assessment of epitaxial graphene production at different manufacturing scales and maturity, J. Ind. Ecol. 21 (5) (2017) 1153–1164, http://dx.doi.org/10.1111/jiec.12526.